AGU100 ADVANCING EARTH AND SPACE SCIENCE

Earth and Space Science

RESEARCH ARTICLE
10.1029/2018EA000369

Special Section:
Science and Exploration of the Moon, Near-Earth Asteroids, and the Moons of Mars

Three-Dimensional Raman Tomographic Microspectroscopy: A Novel Imaging Technique

Mehmet Yesiltas[1], Steven Jaret[2], Jordan Young[2], Shawn P. Wright[3], and Timothy D. Glotch[2]

[1]Faculty of Aeronautics and Space Sciences, Kirklareli University, Kirklareli, Turkey, [2]Department of Geosciences, Stony Brook University, Stony Brook, NY, USA, [3]Planetary Science Institute, Tucson, AZ, USA

Key Points:
- In situ three-dimensional Raman tomographic imaging is performed
- Chemical constituents of terrestrial and extraterrestrial samples and their three-dimensional distributions are presented
- Mineralogical crystallization scenarios can be revealed with this technique

Supporting Information:
- Supporting Information S1
- Movie S1
- Movie S2
- Movie S3
- Movie S4
- Movie S5
- Movie S6
- Movie S7
- Movie S8
- Movie S9
- Movie S10
- Movie S11
- Movie S12
- Movie S13
- Movie S14
- Movie S15
- Movie S16

Correspondence to:
M. Yesiltas,
myesiltas@knights.ucf.edu

Citation:
Yesiltas, M., Jaret, S., Young, J., Wright, S. P., & Glotch, T. D. (2018). Three-dimensional Raman tomographic microspectroscopy: A novel imaging technique. *Earth and Space Science*, *5*, 380–392. https://doi.org/10.1029/2018EA000369

Received 23 JAN 2018
Accepted 3 AUG 2018
Accepted article online 8 AUG 2018
Published online 24 AUG 2018

Abstract Chemical constituents and their spatial distributions in terrestrial and extraterrestrial samples may provide clues to their formation histories and secondary processes they were subjected to. Most analytical tools are either limited in imaging the interior of samples or they are destructive such that the sample is chemically modified. In this work, we have conducted three-dimensional Raman tomographic imaging experiments on both terrestrial and extraterrestrial samples. The in situ nondestructive analytical technique presented here provides spatial distribution of various chemical constituents from the interior of the samples with high spatial and depth resolution. Raman data were first collected from two-dimensional layers at the surface and at various depths inside the samples by means of confocal Raman imaging. Individual chemical distribution maps were generated for each layer, which were then stacked to form and visualize the three-dimensional distributions. In addition to three-dimensional distributions, Raman spectral information was also collected from each pixel within the measured areas, thus allowing us to also perform detailed spectral investigations of the samples.

1. Introduction

Raman spectroscopy is an inelastic scattering analytical technique for molecular identification and characterization, and it has been used for the investigation of variety of samples in different areas of research. In meteoritics and planetary science, Raman spectroscopy is a widely used analytical technique. For instance, Ling et al. (2011) used Raman spectroscopy to investigate lunar soils in the laboratory. Interfaces between chondrules and the matrix of a carbonaceous chondrite were studied by Raman spectral mapping in order to understand the physical processes during the planetesimal formation (Ghimire et al., 2012). Insoluble organic matter extracted from various meteorites has been investigated using Raman spectroscopy in order to assess the degree of primitiveness of organics in meteorites (Busemann et al., 2007). Jaret et al. (2017) used Raman spectroscopy and imaging to investigate the occurrence and distribution of coesite in a shocked silica amygdule in Deccan basalts from Lonar Crater, India. Similarly, Raman spectroscopy has been widely used to identify high-pressure, high-temperature polymorphs in meteroites (Ohtani, 2007).

Although less common in terrestrial geological sciences, Raman spectroscopy is growing in use in these fields as well, particularly for the identification of polymorphs and fluid inclusions (Dubessy et al., 2012, and references therein). Additionally, Raman spectroscopy plays a critical role in diamond anvil cell studies of minerals at high pressures as it is used for a well-established pressure calibration of experiments (Bassett, 2009; Li et al., 2013; Schmidt et al., 2013).

Until recently, Raman spectroscopy has mostly been used in one- or two-dimensional space such that either a Raman spectrum of a point on a sample is collected or intensity distribution maps of an area on the surface of a sample are acquired. By collecting a single Raman spectrum from powdered grains of the Sutter's Mill meteorite, Yesiltas et al. (2014) presented the unusual presence of two distinct carbonaceous phases in this meteorite with different thermal histories. Wang et al. (2015) utilized Raman imaging spectroscopy and reported Raman spectral features of major, minor, and trace species in extraterrestrial as well as terrestrial materials and also presented their spatial correlations to reveal genetic relationships and the geological processes that these materials have experienced. Whereas these studies provide important information and clues, they are limited to the surface of the samples that are under investigation, because both Raman spectra and Raman images are collected only from the surface within the focal plane of the microscope. In these cases, therefore, organic and inorganic compounds below the surface are completely missed and not

Table 1
Experimental Parameters for the Studied in This Work

Experimental parameters	MET 00526	Coesite/glass	Pyrite/calcite	Rutile/quartz	BIF
Measured area (μm^2)	100 × 100	80 × 80	80 × 80	80 × 80	150 × 60
Measured depth (μm)	20	20	30	20	20
Spatial pixel size (μm)	1	0.5	1	0.5	1
Depth pixel size (μm)	0.5	0.5	1	1	1
Integration time (s)	0.05	0.05	0.06	0.05	0.08
Number of layers	40	20	30	20	20
Objective	50X	50X	50X	50X	50X
Grating (grooves per millimeter)	600	600	1800	1800	600
Laser power (mW)	0.2	2.4	2.4	2.4	2.4
Number of Raman spectra	4.0×10^5	1.28×10^5	1.92×10^5	1.28×10^5	1.8×10^5

observed. However, it is highly important in some fields, especially in meteoritics and planetary science, to extract as much information from a sample as possible due to the limited amount and precious state of the samples. Additionally, context of small phases can often provide insight into formation mechanism or process that would otherwise be lost during the investigation of powders or through the analyses of point spectra alone (e.g., Jaret et al., 2017). This goal can be achieved via three-dimensional tomographic investigation. Using three-dimensional Raman tomographic microspectroscopy, the sample of interest can be investigated in situ in three-dimensional space both spatially and spectrally with high resolution at the same time without minimal to no sample preparation.

In this paper, we report the application of three-dimensional Raman tomographic microspectroscopy to study various extraterrestrial and terrestrial samples. Namely, we report Raman tomographic imaging microspectroscopy of an unequilibrated ordinary chondrite Meteorite Hills 00526 (MET 00526), coesite occurrence inside SiO_2 glass from the Lonar Impact Crater in India, pyrite within calcite carbonate matrix from the Shullsburg formation in Wisconsin, rutile occurrence inside quartz from the Pikwitonei granulite of the Superior Province, and a banded iron formation (BIF) that is composed of alternating layers of iron-rich minerals, to cover a range of materials that are of importance in the field of meteoritics and geology. We remark that the extraterrestrial samples that will be returned to Earth in the near future from the primitive asteroids Ryugu and Bennu through Hayabusa2 (Tsuda et al., 2013) and OSIRIS-REx missions (Lauretta et al., 2015), respectively, can also benefit from this technique for the investigation of their chemical compositions.

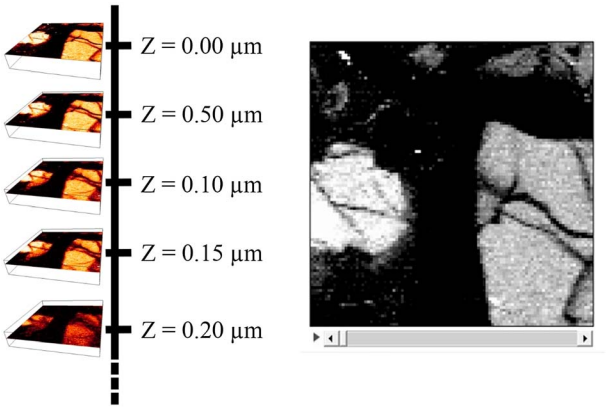

Figure 1. (left) Distribution maps of a chemical component (olivine in MET 00526 meteorite) collected at different depths (*Z*) layer by layer starting from the surface. (right) TIFF image of olivine in the MET 00526 meteorite stacked together using ImageJ software package (Movie S1).

2. Materials and Descriptions

2.1. MET 00526

Meteorites provide invaluable information about the formation and evolution of planetary bodies (Day, 2015; Veronique et al., 2012). We gain significant insights from the organic and inorganic content of meteorites by studying their chemistry in the laboratory. Meteorites are divided into six groups based on their petrology (petrologic types). Meteorites of petrologic types from 1 to 2 are from aqueously altered parent bodies and include substantial secondary mineral components. On the other hand, petrologic types 4 to 6 indicate thermal metamorphism in the parent bodies. Most of the type 3 meteorites were subjected to some thermal metamorphism (much less than types 4 to 6), except type 3.0, which experienced minimum thermal metamorphism. Type 3 meteorites are perhaps the most primitive samples (or least altered) considering that aqueous alteration and thermal metamorphism modify the chemistry of parent bodies. The MET 00526 meteorite is an unequilibrated ordinary chondrite with petrologic type of 3.05 (Grossman & Brearley, 2005). Ordinary chondrites normally lack carbonaceous matter due to parent body processes they underwent

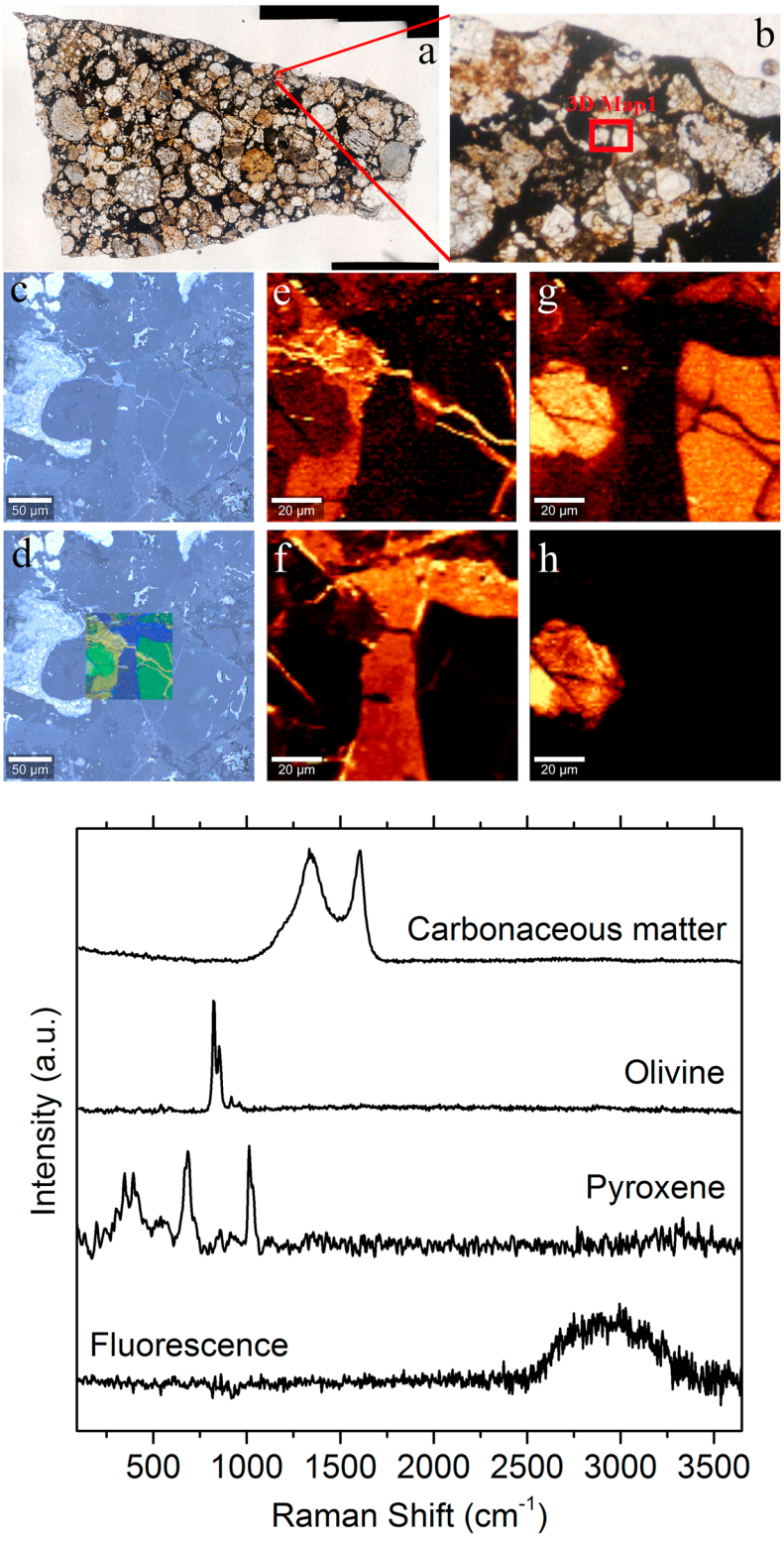

Figure 2. (a) Polarized image of the MET 00526 thin section, roughly ~0.5 cm. Large chondrules of different mineralogy are shown with a dark matrix in the meteorite. (b) Expanded version of the measured region shown with a red square. (c) visible micrograph of the region obtained with a 20X objective. (d) Color-coded distributions of observed components overlayed on the visible image. The colors correspond to the individual components (yellow: pyroxene; green: olivine; blue: carbon). (e–h) Two-dimensional intensity distribution maps of pyroxene, carbonaceous phase, olivine, and high fluorescence region as obtained from the first layer (surface) of the meteorite sample. Among the possibilities for such fluorescence are Fe associated with the olivine or rare-earth element that may be present on the sample. Raman spectra of the components observed in the first layer (surface) of MET 00526 are given in the bottom. See Table 2 for peak positions.

Table 2
Positions of the Observed Raman Peaks and Their Corresponding Assignments

Sample	Raman shift (cm^{-1})	Assignment
MET 00529	1,342; 1,607	Carbonaceous matter
	345; 392; 670; 683; 1,013; 1,030	Pyroxene
	823; 852; 917	Olivine
	643; 670; 825; 1,115; 1,187;1,230; 1,301; 1,457; 1,611; 2,873; 2,910; 2,937; 3,064	Epoxy
Coesite in silica glass	115; 177; 267; 521	Coesite
	250–520; 715	Glass
Pyrite with calcite	337; 370; 419,	Pyrite
	155; 283; 340; 378; 713; 1,087	Calcite
Rutile inside quartz	120; 240; 444; 611; 690	Rutile
	127; 207; 356; 464	Quartz
BIF	173; 295; 1,096	Dolomite
	206; 291; 463; 805; 1,244–1,397	Hematite

and complex formation mechanisms for carbonaceous matter. However, unequilibrated chondrites do contain carbon and other primary chemical components.

We received the MET 00526 meteorite sample from the Antarctic meteorite collection of NASA Johnson Space Center in the form of a thin section. MET 00526 is an unequilibrated ordinary chondrite with carbon-rich matrix and silicate-rich mineralogy. The thin section cut from the meteorite (roughly ~30 μm thick) was glued on a glass slide using epoxy at the NASA's Johnson Space Center. We studied this meteorite for the visualization of various chemical components present in the meteorite sample.

2.2. Coesite Occurrence inside SiO_2 Glass

Coesite is a high-pressure, high-temperature polymorph of SiO_2 that is found in ultrahigh pressure metamorphic rocks (e.g., eclogites, Chopin, 1984) and in impact metamorphosed samples (Chao et al., 1960; Jackson et al., 2016; Jaret et al., 2017; Kieffer, 1971). Coesite can form as a direct solid-state product from quartz (Dachille et al., 1963) or in rare cases can form as the crystallization product from a SiO_2 melt (Chen et al., 2010; Stahle et al., 2008).

The coesite sample is within shocked basalts from the Lonar Crater, India (Jaret et al., 2017; Newsom et al., 2013; Wright et al., 2011). The coesite is located within SiO_2 glass that is itself within basalts that were shocked to Class 2 (Kieffer et al., 1976) or ~25–40 GPa. Coesite and glass are confined only to small (1–3 mm) vesicle fillings, which are interpreted to represent secondary silica precipitates formed prior to the shock event (Jaret et al., 2017). Measurements were acquired on standard polished petrographic thin sections (approximately 30 μm thick).

2.3. Pyrite Within Calcite Matrix

The pyrite sample is from the Blackstone Mine in the Upper Mississippi Valley District (Shullsburg quadrangle) of Wisconsin, composed of Ordivincian to Silurian sandstones and carbonates. These units have been heavily mined for Pb and Zn during the nineteenth century and are well-established regions of mineralization and fluidization (Mullens, 1964). This mine primarily produced sphalerite and galena, with lesser amounts of marcasite, calcite, barite, and pyrite. Rare pyrite occurs as thin layers of euhedral cubes within wall rocks.

2.4. Rutile Occurrence inside Glass

This sample is a large quartz vein in the Pikwitonei granulite domain of the Superior province in Manitoba (Hemming et al., 1994). The quartz contains numerous inclusions of rutile and zircon, with rutile occurring in two size populations: ~500 μm and thinner needles that appear to follow crystallographic orientations.

2.5. BIF

BIF is a term that refers to the sedimentary iron-rich rocks that include layers of iron oxides, silica, and more rarely, other phases. These sedimentary rocks are believed to have deposited during a period of

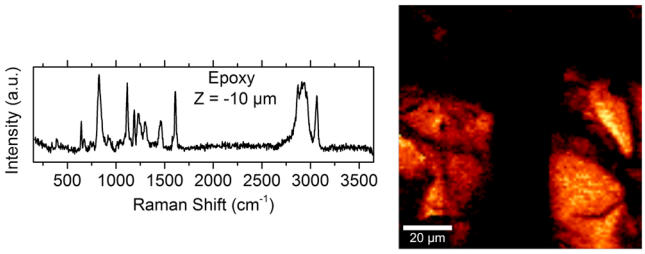

Figure 3. (left) Raman spectrum of the epoxy that appears at $Z = -10$ μm and continues until at least Z = − 20 μm inside MET 00526. (right) Raman distribution map of this component at Z = −10 μm (layer #20).

800 Ma from late Archean to mid-Proterozoic (Klein, 2005). It was reported by Simonson and Schubel (1993) that carbonates were related to the microbial activity in the early history of Earth, and they were associated also with BIFs, and therefore, the BIFs can provide insights for astrobiologically relevant sites and locations on Mars (Crowley et al., 2008). The BIF sample studied here is from the Sherman mine in the Tegami greenstone belt in the Superior Province of Ontario Canada. These Algoma-Type BIFs have an age of ~2700 Ma, adjacent to the slightly younger and more heavily studied Abitibi Greenstone Belt (Ginley, 2016).

3. Experimental Details and Data Analyses

3.1. Technical

We conducted our Raman tomographic imaging experiments at the Center for Planetary Exploration at Stony Brook University, New York, and at the Science and Technology Application and Research Center of Canakkale Onsekiz Mart University, Turkey. Both experimental setups consist of the same instruments, a WiTec alpha300 R (WiTec GmbH) confocal Raman imaging system equipped with a 532-nm Nd:YAG laser, spectrometer with a CCD camera (peltier cooled to −60 °C), and 50X objective (NA = 0.8). The laser power on the sample surface was kept between 0.2 and 2.4 mW measured at the objective to avoid thermal alteration of the samples. After locating a region of interest in the field of view of the microscope, two-dimensional Raman intensity maps of the surface were collected from predefined areas with either 0.5- or 1-μm spatial resolution, and a full Raman spectrum was collected at every pixel within the measured area with ~0.05- to 0.08-s integration time. Experimental parameters set before each data collection session included area to be measured, spatial pixel size desired, integration time, depth to be scanned, and the number of layers desired within the defined depth, which determines the depth resolution. During the data collection, the predetermined area of each layer was measured starting from the surface of the samples down to the deepest layer with either 0.5- or 1-μm depth resolution. Low laser power and very short exposure time resulted no laser-induced damage or heating on the samples. Experimental parameters specific to each studied sample are given in Table 1.

3.2. Data Analyses

Data processing included several steps and software packages. After the data collection, we manually removed the artificial cosmic rays as well as the background. Using WiTec's Project software, chemical distribution maps of individual chemical components were generated by integrating the signal between the endpoints of observed Raman peaks. This procedure was repeated for each layer collected at different depths (Figure 1, left). The distribution maps of all layers were then imported to Fiji-ImageJ software package. Using ImageJ, distribution maps extracted from all layers (40 layers for MET 00526, 30 layers for the pyrite, and 20 layers for the coesite, rutile, and BIF samples) were stacked individually and saved as stacked TIFF images (Figure 1, right), which were then imported to a commercial software package (Avizo) for the visualization of chemical distributions in three dimensions. In Avizo, all components in each sample were color coded and visualized together, and movies of various orientations were generated.

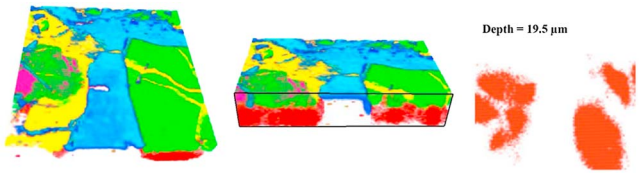

Figure 4. (left) Front view of the reconstruction for MET 00526 (Movie S2). (middle) Clipping-plane cross-section view of the reconstruction (Movie S3). (right) Top view of the reconstruction at 19.5-μm depth, showing the organics at the bottom of the meteorite sample (Movie S4). See supporting information files for movies of the rotations. Colors correspond to the individual components (yellow: pyroxene; green: olivine; blue: carbon; red: contaminant organic matter).

4. Results and Discussions

4.1. MET 00526

A 100-μm × 100-μm area and 20-μm depth from the MET 00526 was measured with 0.5-μm depth resolution and 1-μm spatial resolution, which resulted in 40 layers of Raman data cubes. Using the first layer out of 40 (the top surface layer), we determined the chemical components that are present in the meteorite. The matrix of the meteorite appears to be rich in carbon. While most ordinary chondrites lack carbon, the presence of carbon in the MET 00526 is not surprising considering it is a type 3.05

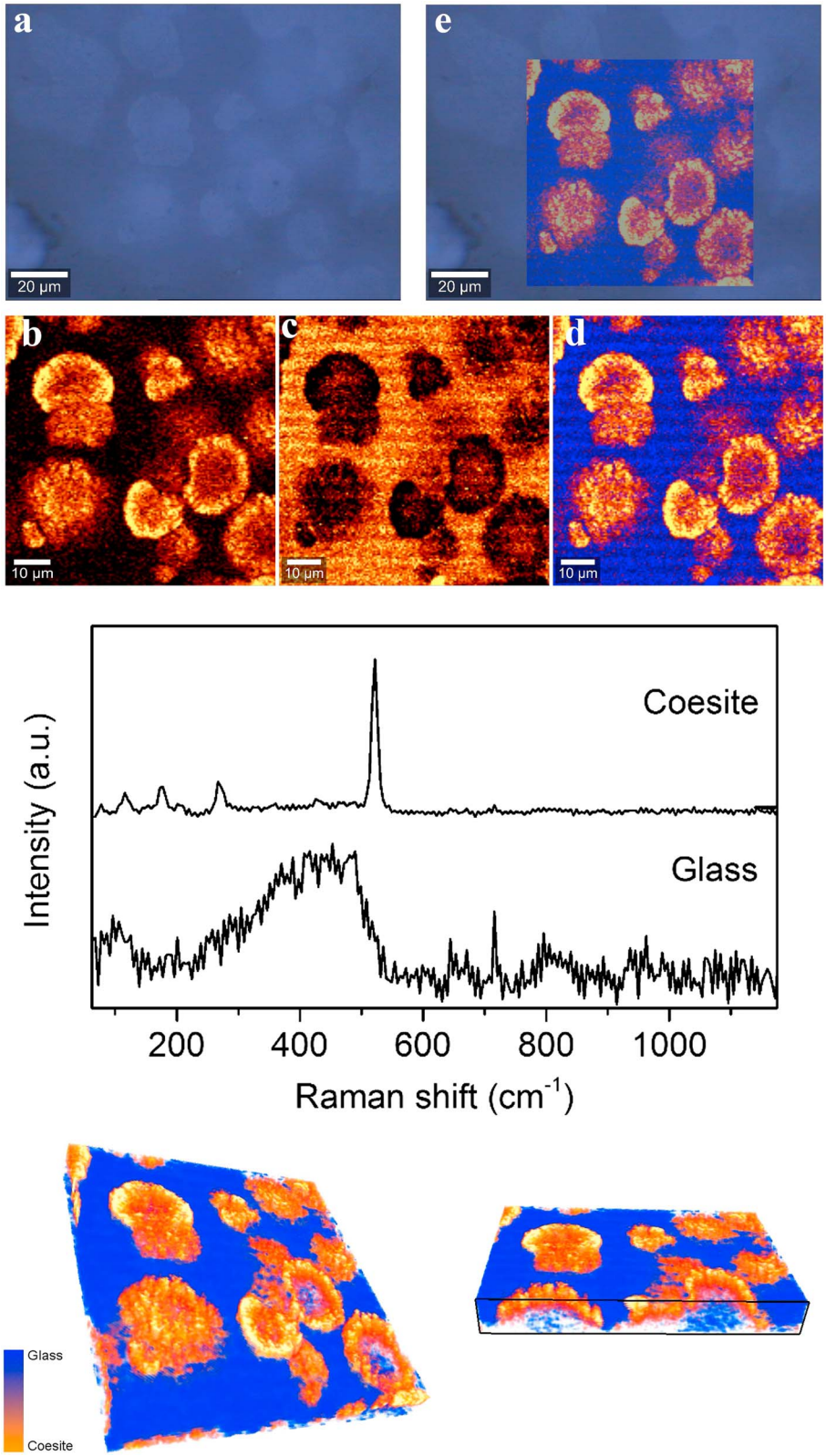

Figure 5. (a) Visible micrograph of the coesite mineral within glass. (b, c) Two-dimensional intensity distribution maps of coesite and glass. (d) Combined distribution map of the two components (yellow/orange is coesite and blue is SiO_2 glass). (e) Combined distribution map overlaid on the visible micrograph. The middle panel presents the Raman spectra of coesite and glass. See Table 2 for peak positions. The bottom panel presents reconstruction of coesite within the glass matrix (Movie S5) on the left, and clipping-plane cross-section view of this reconstruction (Movie S6) in the right. See supporting information files for movies of the rotations.

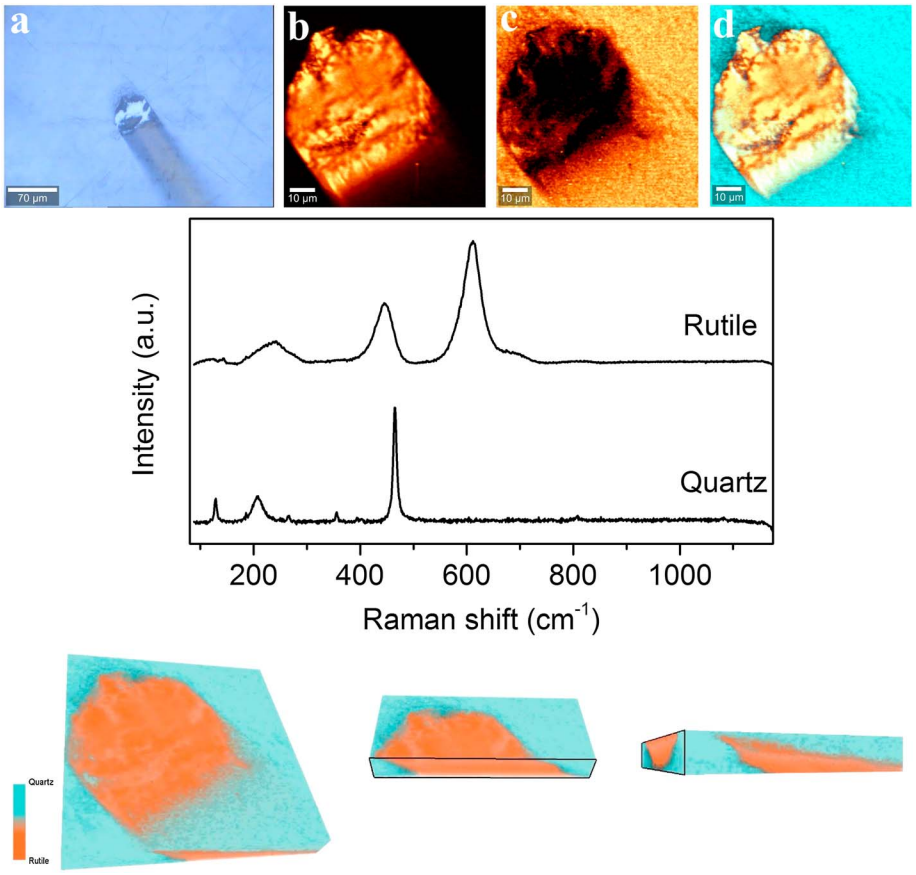

Figure 6. (a) Visible micrograph of the measured sample showing a cylindrical bar of rutile within quartz matrix. The bar of rutile mineral's top surface is on the surface as well (Z = 0 μm) and diagonally goes to deeper inside the quartz matrix. (b, c) Distribution maps of rutile and quartz. (d) Combined distribution map of the two components. The middle panel presents Raman spectra of rutile and quartz. See Table 2 for peak positions. The bottom panel presents reconstruction of the rutile within quartz (Movie S7) on the left, and clipping-plane cross-section views of this reconstruction at different orientations in the middle and right, showing the rutile bar oriented inside quartz matrix diagonally (Movies S8 and S9). See supporting information files for movies of the rotations.

meteorite, and unequilibrated ordinary chondrites normally present relatively higher amounts of carbon. Figure 2 presents reflected plane-polarized light microscope images of MET 00526. We measured a region that contains silicates and carbon-rich matrix, indicated in Figure 2b with a red rectangle. A visible reflected light micrograph of the measured region was collected with our Raman microscope and is shown in Figure 2c. We collected two-dimensional Raman data cubes from an area of 100 μm × 100 μm with 1-μm pixel size and 0.05-s integration time between 100 and 3,700 cm^{-1}. We scanned a depth of 20 μm with 0.5-μm depth resolution, which resulted in 40 layers. Each layer consists of 10,000 pixels, therefore a total of 400,000 Raman spectra were collected for this sample. We generated the two-dimensional chemical distribution maps for these components, as shown in Figures 2e–2h. Figure 2d shows the color-coded distribution of these components overlaid on the visible micrograph to present how and where they are located in the measured area.

Figure 2 also presents Raman spectra of the observed chemical components (see Table 2 for peak positions and their assignments). Raman peaks at 1,341 and 1,601 cm^{-1} are due to disordered (D band) and graphitic (G band) carbon bands, respectively. We also observed the presence of anhydrous silicates such as olivine and pyroxene. A doublet near 845 cm^{-1} is characteristic of olivine. Pyroxene presents Raman peaks near 352, 680, and 1,020 cm^{-1}. Impurities in the sample (Kagan & McCreery, 1994) can intrinsically generate fluorescence due to absorption by the molecule at the wavelength of the laser probe. In the case of MET 00526, the fluorescence appears in the region of 2,500–3,500 cm^{-1} and its Raman spectrum is also shown in Figure 2.

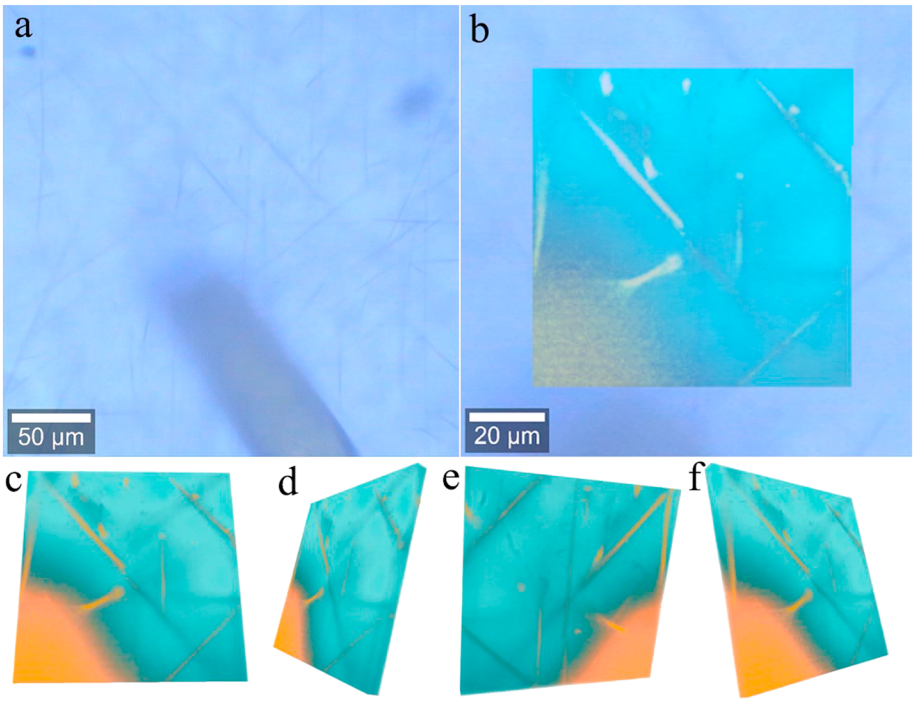

Figure 7. Visible micrograph a of the rutile needles inside the quartz matrix. The measured area b is around the tip of the thick rutile bar shown in (a). The needles are ~0.5 to 1.0 μm thick and ~5 to 20 μm long, randomly oriented inside quartz. (c–f) Reconstruction of the rutile needles within the quartz matrix shown at different orientations (Movie S10). See supporting information files for movies of the rotations.

Using the Raman spectra and distribution images obtained from the first layer, we investigated the succeeding layers and generated the distribution maps of the components for all layers. During the data analyses of the MET 00526 meteorite, another component was observed to appear around 10-μm depth and continue until the depth of 20 μm in our measurement. The Raman spectrum of this component (Figure 3) presents various C-H bending and stretching modes both in the fingerprint region as well as in the higher-frequency region. This component is in fact the epoxy resin used during the sample preparation. The meteorite thin section was prepared by gluing it on a glass slide using epoxy, and it was vacuum impregnated when it was first placed in epoxy. Therefore, it is possible for the epoxy to penetrate into the meteorite sample to this extent (Roger S. Harrington, private communication, May 2016). The analyses of MET 00526 shows that one has to be extra cautious when studying organic compounds in meteorites that are prepared in any way in the laboratory.

We combined distribution maps from all layers using Avizo and generated the three-dimensional tomographic reconstructions of the distributions of all observed components in MET 00526. Figure 4 presents selected 2-D projections of these reconstructions. See supporting information files for movies of the rotations.

4.2. Coesite in Silica Glass

We measured a 80-μm × 80-μm area of the coesite sample with 1-μm depth resolution. The coesite exhibits a strong peak at 521 cm^{-1}, which reflects the Si-O-Si stretching mode. Coesite also exhibits weaker peaks at 113, 173, 267, and 429 cm^{-1}. The SiO_2 primarily exhibits a broad peak near 449 cm^{-1}, with a substantial drop-off in intensity at 494 cm^{-1}. The 2-D and 3-D mapping of this sample shows that the coesite occurs as ~30-micron spherical aggregates that are actually composed of smaller, micron-sized, individual microcrystallites and nanocrystallites. This is particularly apparent in the 3-D maps that show SiO_2 glass underneath many of the coesite grains (Figure 5).

4.3. Rutile Inside Quartz

We measured a 80-μm × 80-μm area on the rutile sample, where the rutile appears as a cylindrical bar that extends into the quartz matrix at an angle (Figure 6). The quartz is identified by the strong peak at

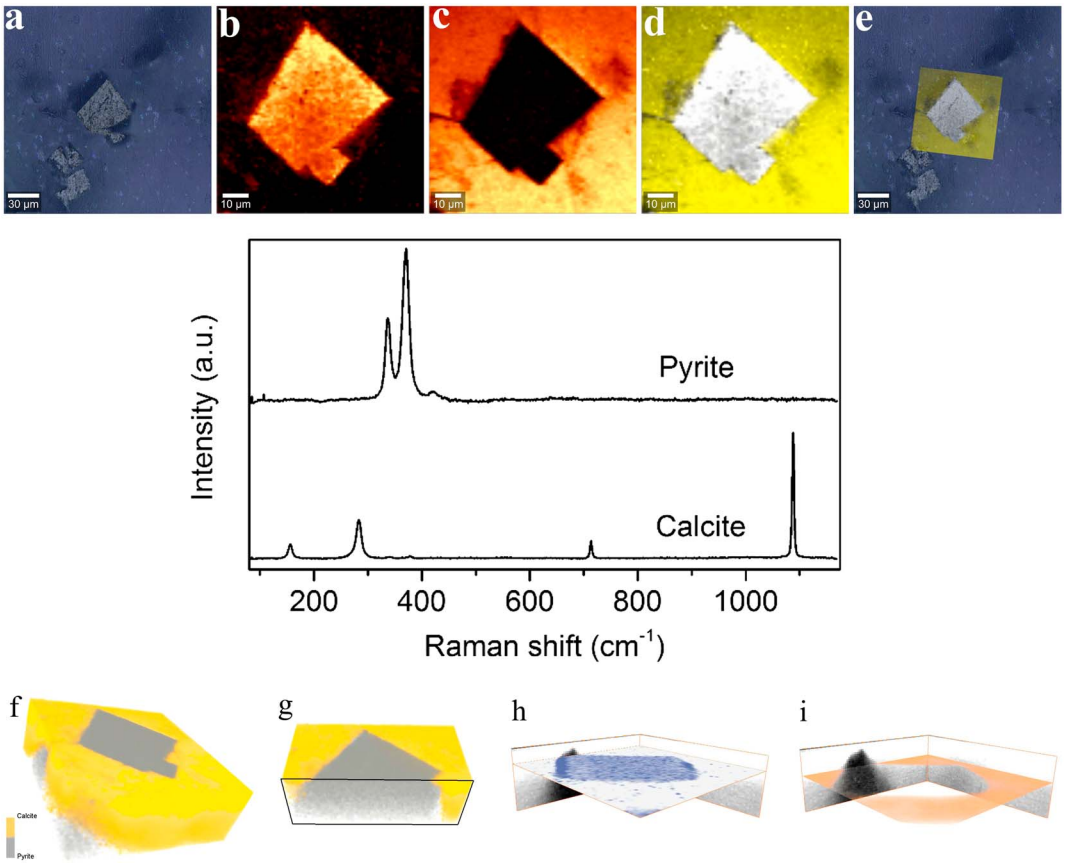

Figure 8. (a) Visible micrograph of the measured pyrite sample within the matrix of carbonate mineral calcite. (b, c) Distribution maps of the pyrite and calcite. (d) Combined distribution map of the two components. (e) Combined distribution map overlaid on the visible micrograph. The middle panel presents Raman spectra of pyrite and calcite. The pyrite spectrum presents characteristic peaks at 337 and 370 cm^{-1}. Calcite has a strong peak at 1,088 cm^{1} and weaker peaks at 713, 283, and 155 cm^{-1}. The bottom panel presents the reconstructions. (f) Reconstruction of the pyrite mineral within the calcite matrix (Movie S11). (g) Clipping-plane cross-section view of the reconstruction (Movie S12). (h, i) Clipping-plane ortho-slide views of pyrite and calcite (Movies S13 and S14). It is clear that the distribution of pyrite expands at deeper regions (Movie S13). See supporting information files for movies of the rotations.

464 cm^{-1} and weaker peaks at 205 and 125 cm^{-1}. Rutile exhibits a strong peak at 612 cm^{-1} and a weaker peak at 447 cm^{-1}. Smaller grains of rutile are identified by the peak at 612 cm^{-1}, but because the rutile needles are smaller than the sampling volume (single pixel) of the Raman, these spectra are not pure. In particular, the mixtures show both the 464-cm^{-1} peak of quartz plus the additional 612-cm^{-1} peak. The 447-cm^{-1} peak in rutile is masked by the 464-cm^{-1} peak from quartz. Although small individual nanocrystals of rutile can be identified by mapping of the 612-cm^{-1} peak, quantification of the amounts and size of the rutile cannot be determined. Mapping in 3-D is useful in this case because it illustrates the 3-D sampling volume of the Raman imaging instrument.

This particular rutile sample also contains many thin needle-like rutile occurrences inside the quartz matrix; they are randomly oriented inside the quartz and are ~0.5 to 1.0 μm in diameter, and 5 to 20 μm in length (Figure 7a). These rutile needles are spatially resolved in high-resolution three-dimensional Raman tomographic imaging experiments. Figures 7c–7f show the 3-D distribution of the needles at different orientations.

4.4. Pyrite Within Calcite

An area of 80 μm × 80 μm was measured to resolve the cubic pyrite crystals in three dimensions. The 3-D mapping clearly shows the cubic shape of the pyrite grain, which is composed of two cubes adjacent to one

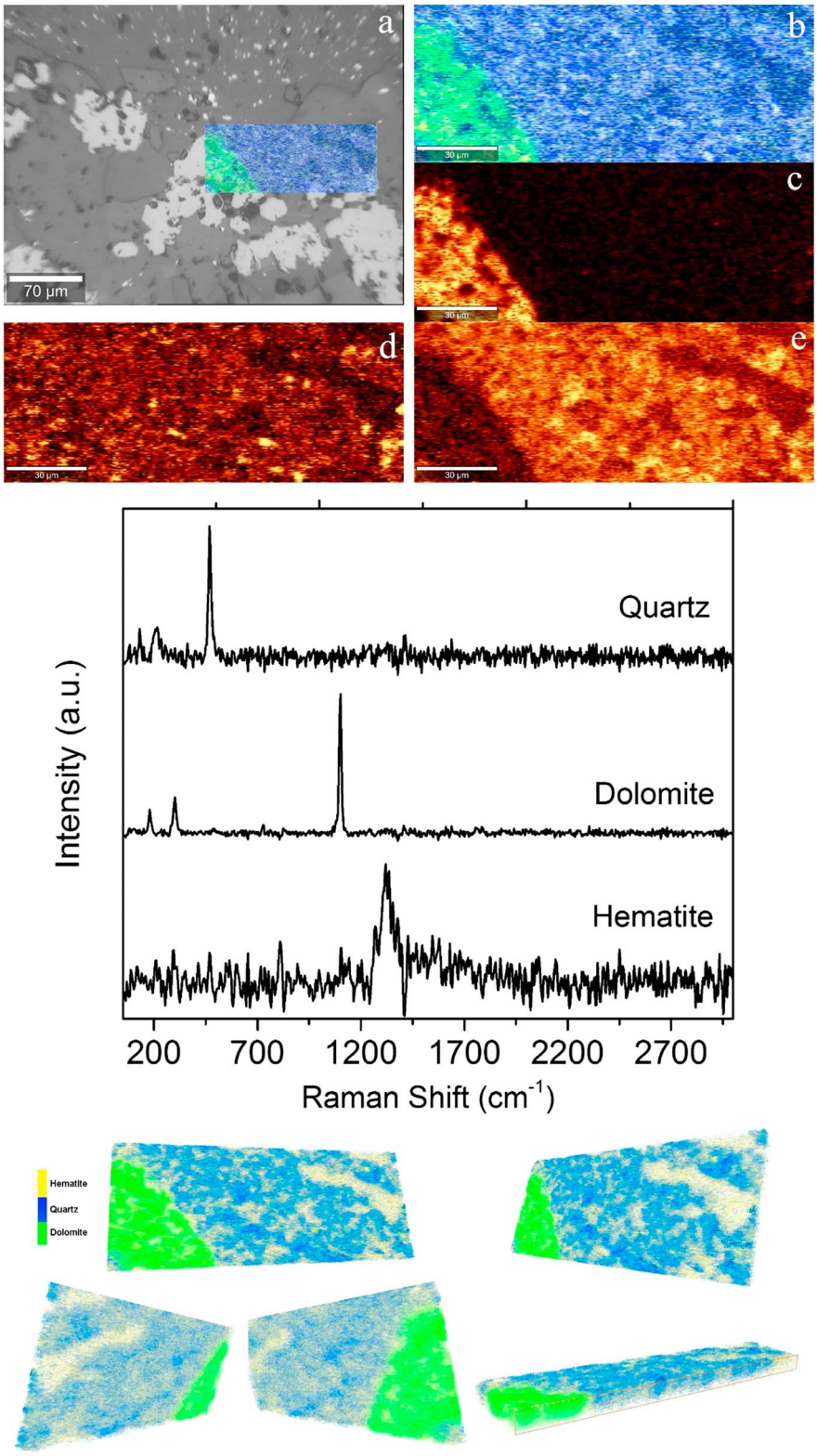

Figure 9. (a) Visible micrograph of the measured BIF sample with the false color combined distribution maps overlaid. Colors correspond to the individual components (green: dolomite; blue: quartz; and yellow: hematite). (b) False color combined distribution map of the components. (c–e) Distribution maps of dolomite, hematite, and quartz, respectively. The middle panel presents Raman spectra of the components observed in the BIF sample. See Table 2 for peak positions. The bottom panel presents reconstruction of the BIF sample shown at different orientations (Movie S15), and the clipping-plane cross-section view of the reconstruction (Movie S16). See supporting information files for movies of the rotations. BIF = banded iron formation.

another inside a calcite matrix. The calcite exhibits a strong peak at 1,088 cm^{-1} and weaker peaks at 713, 283, and 155 cm^{-1} (Figure 8), while pyrite is represented by the two strong peaks at 337 and 370 cm^{-1}. Our 3-D Raman imaging data reveal that the pyrite is pure and did not cocrystallize with other sulfides, which is a common trait of hydrothermal pyrite and distinct from metamorphic pyrite (Craig et al., 1998).

4.5. BIF

We have measured a 150-μm × 60-μm region on the BIF sample and observed the presence of quartz, dolomite, and hematite, whose Raman spectra are shown in Figure 9. Quartz presents a prominent peak at 472 cm^{-1} as well as smaller features near 200 cm^{-1}. The dolomite presents well-known carbonate peaks near 186, 305, and 1,100 cm^{-1}. Hematite is also present in this sample. It has a noisier spectrum, which presents a peak at 1,325 cm^{-1}. The reason for the lower signal-to-noise ratio in the case of hematite is that relatively few pixels were averaged to compose the spectrum.

Figures 9a–9e presents the two-dimensional intensity distribution maps for the observed components. The brigher material near the middle of the visible image (Figure 9a) is dolomite within the silicate (quartz) and iron oxide (hematite) matrix, which are distributed throughout the sample Figure 9 (bottom) presents the images of the three-dimensional distributions at different orientations for a depth of 20 μm.

5. Conclusions

Three-dimensional Raman mapping is a powerful tool for the identification of various organic and inorganic phases in a wide range of terrestrial and extraterrestrial geologic materials. This technique especially has promise in the fields of meteoritics, high-pressure/temperature mineralogy, and for the identification of mineral inclusions because of its ability to spatially map various molecular functional groups and to investigate statistical correlations that can potentially reveal past chemical processes. Three-dimensional textural and chemical observations through this Raman tomographic mapping are particularly useful for our understanding of formation pathways and scenarios as well as parent body alteration processes in the extraterrestrial samples. For instance, spectral parameters of D and G carbon bands can be used to infer peak metamorphic temperatures that the parent asteroid of meteorites experienced; however, since 2-D Raman imaging collects the signal from the surface, such spectral parameters may yield artificially modified parameters because of the modified carbon structures on the surface of samples during the sample preparation. The 3-D tomographic imaging allows the collection of carbon D and G band spectral parameters from the interior of samples where carbon phases have not been altered in any way in the laboratory, thus leading to more correct understanding of the thermal histories of parent asteroids. Organic and inorganic compounds in extraterrestrial materials are not always seen in the surface of thin sections, which is the most common form of meteorite samples; however, deeper regions of the sample may contain valuable compounds that can be easily observed and identified via 3-D Raman imaging. Oxidation processes on newly exposed surfaces of samples can be studied to understand reaction products as well as reaction kinetics and mechanisms. These reactions take place in very short timescales, and with 2-D Raman imaging the data collection is possible after the sample is cut; however, the oxidation reactions starts as soon as the surface is exposed. The 3-D Raman imaging allows the data collection even before the sample is cut to expose the fresh surface such that the oxidation processes and prereactions and conditions can be observed prior to the expose of the interior of the sample to the oxidizing environment.

Similarly, as shown for the rutile sample, the context and orientations of small inclusions can be readily resolved and identified with 3-D imaging. This is important for precious samples where as little cutting of samples is necessary. Three-dimensional imaging can serve as a prescreening technique to better inform where or at what orientation to cut samples if that becomes necessary.

We have demonstrated the application of this novel nondestructive Raman imaging technique to the Antarctic carbonaceous chondrite MET 00526, which revealed the presence of nonindigenous organic material hidden underneath olivine. The carbonaceous phase appears to be distributed within the top 3–5 μm of the sample; however, in some locations it extends to deeper into the sample. The 3-D distribution, morphology, and shape of coesite have been revealed with high resolution in shocked basalts from the Lonar crater in India. The cylindrical rutile bar inside quartz as well as the thin randomly oriented 0.5–1 μm diameter needle-like rutile occurrences inside the quartz matrix have been observed. The 3-D tomography of pyrite in

carbonate shows that the pyrite is composed of two adjacent cubes. The pyrite also appears to be pure and did not cocrystallize with other sulfides, which is a common trait of hydrothermal pyrite and distinct from metamorphic pyrite. Lastly, 3-D Raman mapping reveals the alternating layers of iron in the BIF, which may provide insights for determination of astrobiologically relevant locations due to its association with carbonates that may have been related to the microbial activity in the early history of Earth. The potential of 3-D tomographic imaging has also great potential for broad use such as solid-state devices, electronics as well as medical and biological investigations.

Acknowledgments
We are grateful to NASA's Meteorite Working Group for the meteorite sample from the Antarctic meteorite collection, John Luczaj for the pyrite, Sidney Hemming and Troy Rasbury for the rutile, and Martin Schoonen and Hiroshi Ohmoto (Emeritus at Penn State) for the BIF sample. We thank reviewers and the Editor for their constructive comments. We also wish to thank Volkan Eskizeybek and Arife Aktas (Science and Technology Application and Research Center of Canakkale Onsekiz Mart University, Turkey) for their support during the Raman data collection. This work is funded by the RIS^{4}E node of NASA's Solar System Exploration Research Virtual Institute (SSERVI; PI: T. D. Glotch). The data presented here will be made publicly available via Turkish Spectral Database at http://tsd.klu.edu.tr/.

References

Bassett, W. A. (2009). Diamond anvil cell, 50th birthday. *High Pressure Research*, *29*(2), 163–186. https://doi.org/10.1080/08957950802597239

Busemann, H., Alexander, M. D., & Nittler, L. R. (2007). Characterization of insoluble organic matter in primitive meteorites by microRaman spectroscopy. *Meteoritics & Planetary Science*, *42*(7–8), 1387–1416. https://doi.org/10.1111/j.1945-5100.2007.tb00581.x

Chao, E. C. T., Shoemaker, E. M., & Madsen, B. M. (1960). First natural occurrence of coesite. *Science*, *132*(3421), 220–222. https://doi.org/10.1126/science.132.3421.220

Chen, M., Xiao, W., & Xie, X. (2010). Coesite and quartz characteristics of crystallization from shock produced silica melt in the Xiuyan Crater. *Earth and Planetary Science Letters*, *297*(1-2), 306–314. https://doi.org/10.1016/j.epsl.2010.06.032

Chopin, C. (1984). Coesite and pure pyrope in high-grade blueschists of the Western Alps: A first record and some occurrences. *Contributions to Mineralogy and Petrology*, *86*(2), 107–118. https://doi.org/10.1007/BF00381838

Craig, J. R., Vokes, F. M., & Solberg, T. N. (1998). Pyrite: Physical and chemical textures. *Mineralium Deposita*, *34*(1), 82–101. https://doi.org/10.1007/s001260050187

Crowley, J. K., Hook, S. J., de Souza Filho, C. R., de Pereira Silva, G., Bridges, N. T., Thomson, B. J., et al. (2008). Spectral diversity of terrestrial banded iron formations and associated rocks: Implications for Mars remote sensing. In *Lunar and Planetary Science Conference* (Vol. 39, p. 1263).

Dachille, F., Zeto, R. J., & Roy, R. (1963). Coesite and stishovite: Stepwise reversal transformations. *Science*, *140*(3570), 991–993. https://doi.org/10.1126/science.140.3570.991

Day, J. (2015). Planet formation processes revealed by meteorites. *Geology Today*, *31*(1), 12–20. https://doi.org/10.1111/gto.12082

Dubessy, J., Caumon, M. C., & Rull, F. (Eds.) (2012). *Raman spectroscopy applied to Earth sciences and cultural heritage* (Vol. 12). Twickenham: The Mineralogical Society of Great Britain and Ireland.

Ghimire, B., Dall'Asen, A. G., Gerton, J. M., Ivans, I. I., & Bromley, B. C. (2012, February). Raman spectroscopy investigation in the NWA 3118 meteorite: Implications for planet formation. In American Physical Society Meeting, Abstract K (Vol. 1).

Ginley, S. (2016). A field and petrological study of oxide-facies Algoma-type banded iron formation, Sherman Mine, Temagami, (Master's thesis). University of Ottawa.

Grossman, J. N., & Brearley, A. J. (2005). The onset of metamorphism in ordinary and carbonaceous chondrites. *Meteoritics & Planetary Science*, *40*(1), 87–122. https://doi.org/10.1111/j.1945-5100.2005.tb00366.x

Hemming, S. R., Mezger, K., McLennan, S. M., & Hanson, G. N. (1994). Pb Isotope systematics of large high grade quartz vein, Pikwitonei granulite domain, Manitoba Canada. Abstract of the Eighth International Conference on Geochronology, Cosmochronology, and Isotope Geology.

Jackson, J. C., Horton, J. W., Chou, I.-M., & Belkin, H. E. (2016). Coesite in suevites from the Chesapeake Bay impact structure. *Meteoritics & Planetary Science*, *51*(5), 946–965. https://doi.org/10.1111/maps.12638

Jaret, S. J., Phillips, B. L., King, D. T., Glotch, T. D., Rahman, Z., & Wright, S. P. (2017). An unusual occurrence of coesite at the Lonar crater, India. *Meteoritics and Planetary Science*, *52*(1), 147–163. https://doi.org/10.1111/maps.12745

Kagan, M. R., & McCreery, R. L. (1994). Reduction of fluorescence interference in Raman spectroscopy via analyte adsorption on graphitic carbon. *Analytical Chemistry*, *66*(23), 4159–4165. https://doi.org/10.1021/ac00095a008

Kieffer, S. W. (1971). Shock metamorphism of the Coconino sandstone at Meteor Crater, Arizona. *Journal of Geophysical Research*, *76*(23), 5449–5473. https://doi.org/10.1029/JB076i023p05449

Kieffer S. W., Schaal R. B., Gibbons R., Hörz F., Milton D. J., & Dube A. (1976). Shocked basalt from Lonar Impact crater, India, and experimental analogues. Proceedings, 7th Lunar and Planetary Science Conference (pp. 1391–1412).

Klein, C. (2005). Some Precambrian banded iron-formations (BIFs) from around the world: Their age, geologic setting, mineralogy, metamorphism, geochemistry, and origins. *American Mineralogist*, *90*(10), 1473–1499. https://doi.org/10.2138/am.2005.1871

Lauretta, D. S., Bartels, A. E., Barucci, M. A., Bierhaus, E. B., Binzel, R. P., Bottke, W. F., et al. (2015). The OSIRIS-REx target asteroid (101955) Bennu: Constraints on its physical, geological, and dynamical nature from astronomical observations. *Meteoritics & Planetary Science*, *50*(4), 834–849. https://doi.org/10.1111/maps.12353

Li, J., Chou, I. M., Yuan, S., & Burruss, R. C. (2013). Observations on the crystallization of spodumene from aqueous solutions in a hydrothermal diamond-anvil cell. *Geofluids*, *13*(4), 467–474. https://doi.org/10.1111/gfl.12048

Ling, Z., Wang, A., & Jolliff, B. L. (2011). A systematic spectroscopic study of four Apollo lunar soils. *Journal of Earth Science*, *22*(5), 578–585. https://doi.org/10.1007/s12583-011-0208-3

Mullens, T. E. (1964). *Geology of the Cuba City, new diggings, and Shullsburg quadrangles*. Wisconsin and Illinois: Geological Survey Bulletin 1123-H.

Newsom, H. E., Wright, S. P., Misra, S., & Hagerty, J. J. (2013). Comparison of simple impact craters: a case study of Meteor and Lonar Craters. In G. R. Osinski & E. Pierazzo (Eds.), *Impact Cratering: Processes and Products* (1st ed., pp. 271–286). West Sussex, UK: Blackwell Publishing Ltd.

Ohtani, E. (2007). GSA special paper 421. Advances in High-Pressure Mineralogy.

Schmidt, C., Steele-MacInnis, M., Watenphul, A., & Wilke, M. (2013). Calibration of zircon as a Raman spectroscopic pressure sensor to high temperatures and application to water-silicate melt systems. *American Mineralogist*, *98*(4), 643–650. https://doi.org/10.2138/am.2013.4143

Simonson, B. M., Schubel, K. A., & Hassler, S. W. (1993). Carbonate sedimentology of the early Precambrian Hamersley Group of Western Australia. *Precambrian Research*, *60*(1–4), 287–335. https://doi.org/10.1016/0301-9268(93)90052-4

Stahle, V., Altherr, R., Koch, M., & Nasdala, L. (2008). Shock induced growth and metastability of stishovite and coesite in lithic clasts from Suevite of the Ries impact crater (Germany). *Contributions to Mineralogy and Petrology*, *155*(4), 457–472. https://doi.org/10.1007/s00410-007-0252-2

Tsuda, Y., Yoshikawa, M., Abe, M., Minamino, H., & Nakazawa, S. (2013). System design of the Hayabusa 2—Asteroid sample return mission to 1999 JU3. *Acta Astronautica*, *91*, 356–362. https://doi.org/10.1016/j.actaastro.2013.06.028

Veronique, D., Doris, B., Philippe, C., Vinciane, D., Emmanuelle, J., Steven, G., et al. (2012). From meteorites to evolution and habitability of planets. *Planetary and Space Science*, *72*(1), 3–17. https://doi.org/10.1016/j.pss.2012.05.018

Wang, W., Korotev, R. L., Jolliff, B. L., & Ling, B. (2015). Raman imaging of extraterrestrial materials. *Planetary and Space Science*, *112*, 23–34. https://doi.org/10.1016/j.pss.2014.10.005

Wright, S. P., Christensen, P. R., & Sharp, T. G. (2011). Laboratory thermal emission spectroscopy of shocked basalt from Lonar Crater, India, and implications for Mars orbital and sample data. *Journal of Geophysical Research*, *116*, E09006. https://doi.org/10.1029/2010JE003785

Yesiltas, M., Kebukawa, Y., Peale, R. E., Mattson, E., Hirschmugl, C. J., & Jenniskens, P. (2014). Infrared imaging spectroscopy with micron resolution of Sutter's Mill meteorite grains. *Meteoritics and Planetary Science*, *49*(11), 2027–2037. https://doi.org/10.1111/maps.12321